Geophys. J. Int. (2000) **143,** 898–908

Determination of earthquake energy release in the Eastern Mediterranean region

A. Hofstetter and A. Shapira

Seismology Division, the Geophysical Institute of Israel, PO Box 182, Lod 71100, *Israel*

Accepted 2000 July 18. Received 2000 July 17; in original form 1999 January 12

SUMMARY

Seismic energy radiated by earthquakes in the Eastern Mediterranean region is estimated using the short-period (50 samples per second) seismic recordings made by the Israel Seismic Network during 1990–1997. Our data set is the whole *S*-wave window (from S_n until L_g falls to less than twice the noise level) from 133 earthquakes with a high signal-to-noise ratio. We obtained the attenuation function $(1.850 \pm 0.005) \log R + (0.00460 + 0.00005)R \log e + 0.05$, where the distance range is $50 \leq R \leq 1500$ km. We tested the dependence of the attenuation function on the azimuth and the distance. Despite the different propagation paths of the waves travelling through the continental crust of the Arabian Shield to the east or the intermediate crust of the Mediterranean Sea to the west, we show that from a statistical point of view the attenuation functions are similar. The energy estimation involves time-domain integration of the squared ground-motion velocity, assuming that the attenuation is known, following the method of Kanamori *et al.* (1993). For the magnitude range $3.0 \leq m_B \leq 6.2$ (magnitude determined by the National Earthquake Information Service, NEIS), we obtained the magnitude–energy relationship $\log E_0 = (2.09 \pm 0.10)m_B + (8.86 \pm 0.42)$. Comparison of the seismic energy and the seismic moment suggests that $E \propto M_0^{0.19}$ and that Orowan's stress drop increases as $M_0^{0.19}$. A refinement of the results is expected with the application of the method of Mayeda & Walter (1996) for energy estimation from coda envelopes using a large data set of broad-band observations.

Key words: attenuation, earthquakes, Eastern Mediterranean, energy release.

INTRODUCTION

The energy release of an earthquake is an important physical quantity that describes the earthquake. Many studies, employing various methods, have attempted to use the observed seismograms for the estimation of seismic energy (e.g. Gutenberg & Richter 1942, 1956a,b; Bath 1966; Thatcher & Hanks 1973; Boatwright & Choy 1986; Singh & Ordaz 1994; Lindenfeld & Berckhemer 1995; Mayeda & Walter 1996). Shaw (1998) examined the scaling of radiated energy as a function of moment and rupture length, assuming various simple elasto-dynamic fault models. A commonly used energy–magnitude relationship is $\log E_S = 1.5M_S + 11.8$, where E_S is in ergs and M_S is the surface wave magnitude (Gutenberg & Richter 1956a). Recently, Kanamori *et al.* (1993) presented a method for the estimation of the seismic energy based on time-domain integration of local and regional velocity-squared seismograms observed at TERRAscope in southern California. They were able to obtain reliable energy estimation, since the propagation effect is of minor importance at short distances.

Although broad-band digital recordings of local and regional earthquakes have become more common in the Middle East and the Eastern Mediterranean region, there is a wealth of short-period digital recordings, made over a longer time period, and from sources more numerous and better distributed in azimuth and epicentral distance than the rather limited data set of the broad-band observations. Thus we take advantage of the large short-period data set in estimating the energy of local and regional observations (Fig. 1a), which includes small to moderate events as well. As a consequence of the wealth of short-period observations, we can be very selective in choosing only high-quality data. Our energy estimation, as explained below, is based on the method of Kanamori *et al.* (1993) using short-period data.

Recently, Mayeda & Walter (1996) proposed estimating the energy from the coda envelopes using broad-band data at different frequency ranges. The method of Mayeda & Walter (1996) is indeed better than that of Kanamori *et al.* (1993). However, one can still get an insight into earthquake energy release in the Eastern Mediterranean region using the short-period data, although a refinement of the results is expected when applying the method of Mayeda & Walter (1996) using a large data set of broad-band observations.

A pre-requisite for reliable energy estimation is the detailed

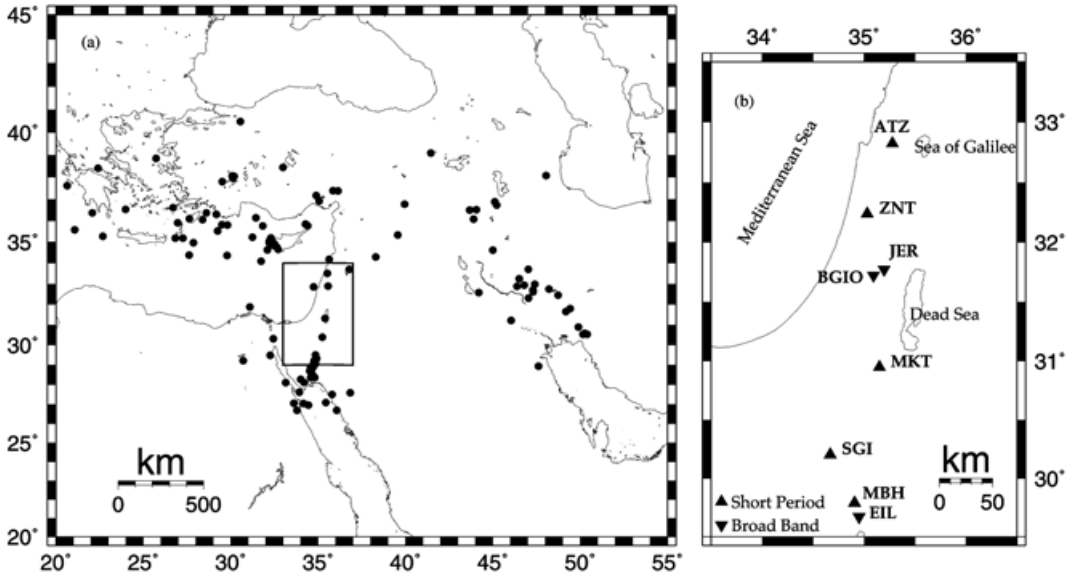

Figure 1. (a) Geographical distribution of earthquakes that were used in this study. (b) Location (rectangle in part a) of the three-component short-period seismic stations (solid triangle) and the broad-band stations (inverted triangle).

knowledge of the velocity and attenuation structure. Recent seismic refraction studies of the crust of Israel and Jordan (Ginzburg & Gvirtzman 1979; Ginzburg *et al.* 1979a,b; Makris *et al.* 1983; El-Isa *et al.* 1987; El-Isa 1990) support the view that Israel is a transition zone between the thick continental crust of the Arabian Shield and the relatively thin oceanic or intermediate crust under a relatively thick sedimentary layer of the Eastern Mediterranean Sea (Makris *et al.* 1994).

The goal of this study is to estimate the energy of earthquakes in the Eastern Mediterranean region based on the short-period seismograms recorded by the Israel Seismic Network. Our basic assumption is that the seismic energy estimation, proportional to the integral of the velocity squared, using the method of Kanamori *et al.* (1993) is valid for short distances (up to about 400 km). We empirically determine the distance dependence of the attenuation function, up to a distance of about 1500 km. If the method of Kanamori *et al.* (1993) is valid for short distance, and knowing the dependence of the attenuation on the distance, then we argue that the seismic energy of earthquakes is given by

$$K\ (\text{integral of } v^2) + (\text{attenuation correction})\,, \qquad (1)$$

where K is a constant and v is the velocity. The first term is the Kanamori *et al.* (1993) term and the second is a result of the attenuation property. The validity of the extension of the distance range, for the estimation of the attenuation function, from about 400 km to about 1500 km is extensively discussed below. In the next step we define the seismic energy, based on short-period observations, whilst incorporating the attenuation function. Finally we show the various empirical relationships between the energy and several seismic parameters such as magnitude and seismic moment.

DATA AND ACQUISITION SYSTEMS

Seismicity in Israel is monitored by the Israel Seismograph Network (ISN; GII Seismological Bulletins 1984–1998), which includes five three-component short-period stations (Fig. 1b, Table 1). Each station is equipped with a 1 Hz natural frequency seismometer, with an effective frequency range from 0.4 Hz up to about 20 Hz. A general description of a short-period station is given by Lee & Stewart (1981), and a similar description of a typical ISN station is given in GII Seismological Bulletins (1984–1998) and by van Eck & Hofstetter (1989). The first ISN broad-band station was installed in 1994. At the beginning of 1999 three broad-band stations operated routinely (Fig. 1b). Each station is composed of a STS2 seismometer with a Quanterra data logger, with a flat response in the frequency range 0.001 Hz to almost 100 Hz. The number of high-quality recordings of broad-band stations that can be used for seismic energy calculation is small, in contrast to the number of short-period recordings (Table 2). Therefore, data of the broad-band stations are used as a complementary source to the short-period observations only in the later stage of the analysis, i.e. seismic moment estimation, and not for the attenuation function.

Table 1. ISN stations that were used in this study. Names in italics represent broad-band stations.

Station	Latitude (north)	Longitude (east)	Z (km)	Station correction
ATZ	32.824	35.278	0.515	1.07
BGIO	31.722	35.092	0.760	
EIL	29.670	34.951	0.200	
JER	31.772	35.197	0.770	
MBH	29.791	34.907	0.842	0.62
MKT	30.948	35.151	0.517	0.83
SGI	30.204	34.668	0.560	0.49
ZNT	32.238	35.031	0.313	2.75

During 1990–1997 we selected 133 events, based on the catalogue of NEIS, with a high signal-to-noise ratio at a distance range of up to 1500 km (Fig. 1a); the NEIS body wave magnitude range is $3.0 \leq m_B \leq 6.2$. Observed earthquakes with a poor signal-to-noise ratio or doubtful identification were rejected (Table 2). We use the body wave magnitude as determined by

Table 2. List of earthquakes that were used in this study. For illustrative purposes only, Δ and δ are the distance and azimuth relative to the centre of the network (approximately BGIO in Table 1). Event names in italics (mainly in 1997) represent cases in which we used broad-band observations in addition to short-period observations.

Event yrmodyhrmn	Latitude °N	Longitude °E	Depth km	m_B	δ	Δ km	E_0 erg	M_0 dyn cm
9002200555	32.592	44.204	37	4.6	81	849	3.8e19	0.7e23
9005241512	32.944	46.801	58	4.9	79	1094	2.4e19	0.2e24
9008031157	32.758	48.213	45	5.0	81	1225	1.2e20	1.1e24
9106192317	33.703	47.037	10	4.6	75	1125	6.6e17	0.1e24
9107051352	36.727	45.219	11	4.8	56	1070	4.2e17	0.2e24
9107212016	36.882	45.118	33	4.3	55	1070	2.1e18	0.2e24
9107240945	36.520	44.066	25	5.4	54	969	3.5e20	2.2e24
9110181648	33.702	36.792	10	4.9	33	260	1.9e18	3.7e22
9110311435	30.541	50.163	24	4.9	91	1426	6.4e20	0.3e25
9111101519	30.585	50.268	43	5.0	91	1436	1.9e20	0.2e25
9212110925	32.892	46.391	53	4.8	80	1056	8.0e18	0.7e23
9212201037	36.078	43.896	33	4.4	56	931	1.7e18	0.5e23
9301151215	36.495	43.676	33	4.7	53	938	3.7e19	0.1e24
9301231038	32.988	47.411	33	4.7	79	1151	1.5e19	0.2e24
9302012241	33.255	46.517	88	4.7	78	1071	1.6e18	0.5e24
9306022201	28.940	47.606	10	4.7	101	1227	1.4e19	0.3e24
9306141245	32.717	47.298	33	4.8	81	1139	2.5e19	0.3e24
9409271432	31.661	49.176	41	4.5	86	1318	3.4e19	0.2e24
9411201431	35.335	39.557	28	5.1	44	563	2.7e20	1.2e24
9412030602	32.624	47.307	80	4.6	81	1140	1.9e20	0.1e25
9501010851	30.543	50.396	42	4.8	91	1448	1.1e20	0.2e25
9501050153	28.110	33.150	6	3.4	207	451	1.6e16	6.8e20
9501080219	38.440	32.980	6	4.4	345	770	4.4e17	1.8e22
9501090332	29.070	34.740	33	3.5	189	301	2.8e15	5.7e20
9501121332	32.860	34.740	9	3.0	338	132	5.6e15	9.5e20
9501151707	28.360	34.820	2	4.1	186	377	7.8e15	1.3e21
9501210348	37.378	36.151	27	4.5	7	629	4.1e17	1.7e22
9502041903	35.818	29.502	43	4.1	311	697	5.4e16	1.5e22
9502062115	28.930	34.740	33	3.6	189	316	7.3e15	2.3e21
9502101512	29.230	34.780	11	3.5	189	282	1.6e15	3.8e20
9502141247	35.849	34.286	33	4.4	349	463	1.2e18	9.4e21
9502141338	35.770	34.410	6	3.4	350	452	8.6e16	2.2e21
9502181321	29.080	34.850	4	3.7	187	298	2.3e15	6.3e20
9502191836	27.090	35.450	6	3.4	177	516	1.9e16	1.6e21
9502210356	36.089	27.635	46	4.0	306	852	2.1e17	2.2e22
9502232103	35.046	32.279	10	5.8	323	458	2.6e20	8.1e24
9502232110	34.660	32.720	4	4.6	324	399	1.1e19	9.2e22
9502232140	35.043	32.314	10	5.3	324	455	1.8e19	2.0e23
9502232143	34.970	32.210	25	4.3	322	455	5.0e17	1.8e22
9502232159	35.050	32.340	25	4.1	324	455	1.4e17	7.0e21
9502232212	35.201	32.304	10	3.8	325	470	1.6e17	4.8e21
9502232230	35.114	32.325	10	4.0	324	461	8.0e16	3.3e21
9502232351	35.125	32.329	22	4.0	324	462	2.6e17	5.3e21
9502240008	34.860	32.450	25	4.0	323	432	3.6e16	2.3e21
9502240027	34.840	32.530	6	4.5	324	426	1.2e19	2.2e22
9502240132	35.149	32.277	10	3.7	324	467	6.1e16	1.6e21
9502240242	34.910	32.510	25	3.0	324	433	7.6e15	6.6e20
9502240252	34.990	32.290	25	3.1	323	452	2.5e16	9.1e20
9502241149	35.087	32.334	10	3.3	324	458	3.6e16	1.8e21
9502242023	34.850	32.450	4	4.0	323	431	6.1e16	2.4e21
9502242142	34.900	32.280	25	3.1	322	445	9.2e15	1.3e21
9502242213	34.860	32.450	4	3.0	323	432	1.0e16	1.3e21
9502250047	35.055	32.348	10	3.3	324	455	3.0e16	7.6e20
9502250214	35.129	32.320	18	3.9	324	463	1.7e17	2.0e20
9502251214	34.880	32.260	25	3.0	322	444	1.1e16	7.5e20
9502260453	35.031	32.196	11	4.2	322	461	3.8e17	3.8e21
9502260836	27.040	34.170	5	4.6	191	532	5.2e18	2.2e22
9502270623	35.232	31.240	10	4.4	317	536	2.2e17	7.5e21
9502281256	36.305	29.176	57	4.1	313	754	3.0e17	1.2e22
9503010747	36.770	39.950	10	4.4	36	705	1.1e18	2.8e22
9503012058	34.760	32.640	5	3.1	324	412	2.0e16	7.7e20

Table 2. (*Continued.*)

Event yrmodyhrmn	Latitude °N	Longitude °E	Depth km	m_B	δ	Δ km	E_0 erg	M_0 dyn cm
9503050142	35.010	32.320	25	3.2	323	452	3.2e16	1.0e21
9503110904	34.621	44.996	33	4.3	68	962	1.2e18	0.6e23
9503150920	27.617	33.933	10	3.8	195	475	1.3e18	8.2e22
9504010448	31.223	46.051	33	4.6	90	1027	6.6e18	9.7e22
9504050752	34.382	27.627	26	4.5	294	769	3.0e18	2.6e22
9504060524	27.050	33.620	5	4.2	197	544	2.4e17	3.1e21
9504080825	36.140	31.442	70	4.1	325	600	3.5e17	8.2e21
9504132023	37.390	35.860	3	4.9	4	628	5.4e17	5.6e22
9504180612	31.802	49.426	18	4.9	86	1341	4.1e19	0.6e23
9504190104	36.051	28.380	87	3.9	308	794	4.8e17	0.2e23
9504201041	26.690	36.070	1	4.2	171	566	9.0e16	5.6e21
9504220021	30.892	49.908	25	5.1	90	1397	1.2e20	9.8e23
9504230132	33.510	35.530	33	4.1	7	196	3.5e17	4.0e21
9504242317	37.169	34.893	33	4.4	356	602	1.4e17	1.1e22
9504261000	34.180	35.640	11	4.1	7	271	1.7e17	3.1e21
9504280625	34.966	27.869	23	4.3	299	773	5.3e17	2.3e22
9505081908	32.900	35.570	2	3.0	13	131	3.6e15	2.3e20
9505111313	34.920	32.430	25	3.1	324	438	3.0e16	1.0e21
9505140400	28.374	34.585	10	4.3	189	379	1.3e19	1.8e23
9505140437	28.470	34.700	4	3.6	188	367	8.1e15	1.2e21
9505140702	27.510	35.800	4	4.3	173	472	8.4e16	6.0e21
9505230303	35.274	22.673	16	4.5	291	1230	3.8e19	1.2e23
9505290458	35.039	32.246	10	5.3	323	459	3.5e19	1.1e23
9506021049	35.190	26.830	25	3.6	298	870	2.7e17	1.2e22
9506072309	32.461	48.737	33	5.0	82	1274	4.6e19	0.9e24
9506092330	28.630	34.610	2	4.2	190	351	4.3e16	8.9e21
9506220526	36.910	35.058	42	4.1	358	572	6.1e16	3.2e21
9506270550	35.800	29.810	25	3.2	313	674	4.7e15	5.0e21
9506280332	28.280	34.010	5	3.5	197	402	7.8e16	6.5e20
9506300534	36.366	28.609	48	3.9	311	798	1.3e17	2.2e22
9507030034	39.086	41.461	33	4.3	32	989	1.2e18	4.1e24
9507080317	29.220	30.720	6	3.7	238	517	1.8e17	3.6e21
9508092030	26.690	33.790	6	4.0	194	578	5.2e16	1.0e22
9508151108	36.532	23.987	93	3.9	300	1165	4.1e18	9.9e22
9508180544	37.802	29.517	10	4.2	323	851	6.5e17	8.8e22
9508220534	36.609	26.708	168	5.1	306	953	8.9e18	2.7e23
9508250525	31.320	35.410	19	3.2	162	50	1.3e16	6.7e20
9508262042	34.630	32.100	25	3.5	318	433	2.2e16	3.6e21
9508281315	40.490	30.560	5	4.9	337	1057	1.1e19	1.8e23
9508312305	29.280	34.870	6	4.0	187	276	6.5e15	1.9e21
9509010256	29.320	34.910	3	3.4	186	271	1.5e15	4.4e20
9509081213	29.489	32.256	10	3.9	229	380	6.8e17	6.6e21
9509140553	27.590	36.840	5	4.1	161	485	3.8e16	1.9e21
9509181429	35.523	29.247	73	4.5	308	696	1.1e18	3.5e22
9509182219	32.314	47.051	33	4.3	83	1115	1.9e18	1.8e23
9509242316	26.960	34.450	5	4.1	188	536	2.1e16	2.9e21
9509261458	38.040	30.195	20	4.8	327	836	2.0e18	1.5e23
9510012221	38.063	30.093	33	4.4	327	843	1.7e17	1.1e23
9510031454	28.120	34.190	5	4.1	194	415	1.1e16	6.7e21
9510051615	37.961	30.131	33	4.7	327	832	5.8e17	2.2e23
9510061616	38.000	30.146	33	4.4	327	835	6.7e17	1.1e23
9510170614	30.320	32.430	7	3.3	240	312	1.0e16	9.7e20
9510200305	35.189	27.267	33	3.9	299	833	1.7e17	1.8e22
9510211400	35.760	31.830	25	3.0	325	545	2.2e16	5.9e21
9510310342	34.370	29.790	25	4.5	301	586	2.6e18	6.6e22
9511220415	28.826	34.799	10	6.2	7	330	6.1e22	7.2e26
9511230522	30.400	35.240	9	3.4	180	149	4.7e15	1.4e21
9511240332	31.890	31.090	5	4.1	273	394	2.9e18	2.5e21
9512010917	28.700	34.523	10	4.4	191	345	1.3e18	4.2e22
9512061757	28.862	34.679	10	4.0	189	324	1.1e18	7.2e22
9512080412	28.919	34.651	10	4.4	190	319	1.3e18	3.4e22
9512110132	28.878	34.690	10	5.0	189	322	2.6e18	4.0e23
9512220549	29.510	34.860	9	3.5	188	251	1.3e15	3.7e20

Table 2. (*Continued.*)

Event yrmodyhrmn	Latitude °N	Longitude °E	Depth km	m_B	δ	Δ km	E_0 erg	M_0 dyn cm
9512312242	35.909	26.965	35	4.6	303	894	5.7e17	2.2e22
9612242216	34.30	38.31	29	5.1	46	414	3.2e20	2.6e24
9701131019	34.09	31.74	33	5.3	311	408	3.1e20	1.1e24
9702281257	38.075	48.050	10	5.5	56	1375	9.2e20	3.8e26
9707271007	35.582	21.064	33	5.5	292	1367	2.8e20	1.7e25
9710131339	36.379	22.071	24	6.2	297	1305	4.2e21	3.3e25
9711052110	38.416	22.403	10	5.6	306	1372	1.6e19	9.4e24
9711142138	38.855	25.735	33	5.8	316	1160	1.6e20	8.8e24
9711181307	37.618	20.638	33	5.9	300	1473	4.7e21	2.2e26

NEIS, assuming that it is based on many stations in the case of moderate to strong events. We added observations that were not reported by NEIS, but were clearly observed by the Israel Seismic Network (ISN). Normally these were local events ($\Delta < 400$ km) with relatively low magnitude ($m_B < 4.0$), where the magnitude determination (Shapira 1988) is based on coda measurements. The $m_{B\ ISN}$ is calibrated to be equal to $m_{B\ NEIS}$ (Shapira 1988). During this period, a strong earthquake ($M_W = 7.2$) occurred in the Gulf of Aqaba and was followed by an intense earthquake swarm. In order to avoid biasing the result, we use only the main shock on 1995 November 22 and the four strongest aftershocks that occurred shortly afterwards.

The propagation of S_n and L_g waves in the Eastern Mediterranean region is rather complex, including areas of efficient and inefficient paths (Rodgers *et al.* 1997; Sandvol *et al.* 1998; Thio *et al.* 1998). Generally the Mediterranean Sea and the Red Sea are characterized by inefficient L_g propagation, whilst the Arabian Shield is characterized by an efficient path. Efficient S_n propagation is found for the surrounding regions of the Arabian Shield and the Mediterranean. Inefficient S_n propagation coincides with a zone of low P_n velocity, that is, the Turkish and northern Iranian plateaux or across the Dead Sea fault. Fig. 2 illustrates an event that was observed at the station MKT E–W component, located at about 630 km away from the earthquake (event no. 19, Table 2). The manually determined window (between S1 and S2) includes all the energy of the S_n and L_g waves until the amplitude of the signal is essentially the same as that of the background noise (signal-to-noise ratio, SNR < 2). The signal shows poor S_n and efficient L_g propagation in agreement with the observations of Rodgers *et al.* (1997), Sandvol *et al.* (1998) and Thio *et al.* (1998).

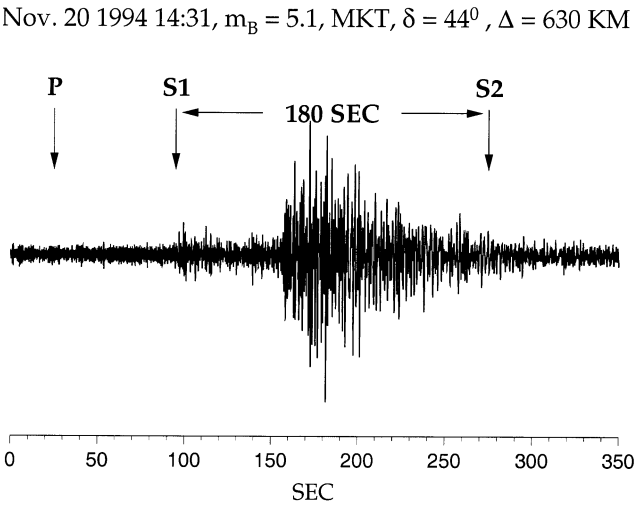

Figure 2. An example of the data used, which were observed at station MKT, E–W component, located at about 630 km away from the epicentre (event no. 19 in Table 2). P denotes the P phase, S1 and S2 define the starting and endpoints of the window used for the energy estimation.

ATTENUATION FUNCTION

Our first step is to estimate empirically the attenuation as a function of the distance, in the frequency band of the short-period observations (right term in eq. 1). In the following step we determine the seismic energy. We assume that in this frequency band the attenuation is a property of the medium and is independent of the magnitude of the earthquakes and the azimuth. This simplifying assumption can be erroneous, since with an m_B range of roughly 3–6 there is potential for a significant range in the dominant signal frequency, which may affect the attenuation function. Below we conduct several tests to check the validity of this assumption. For a given event, observed by a series of stations, we search for an attenuation curve that provides the best fit to the seismic energy–distance relationship. It is a relationship of the type $n \log R + kR \log e + \log s_i$, where k and n are constants, R is the hypocentral distance ($R^2 = \Delta^2 + h^2$) in the distance range of $50 \le R \le 1500$ km, Δ is the epicentral distance, h is the source depth (5–20 km for most of the events; estimated error depth is less than 10 km), s_i is the station correction (Table 1) of the ith station, $i = 1, 2, \ldots N_s$, and N_s is the number of stations. Since we assume that the attenuation is independent of the magnitude, in the frequency band of the short-period observations, we obtain a set of parallel curves, all having the same attenuation property. Essentially, the attenuation curve is determined using many points from a relatively short distance of about 50 km to a far distance of up to 1500 km, which in turn assures the validity of our assumption. The distribution of these observation points with distance is fair and sufficient to obtain an unbiased and reliable estimate of the earthquake energy. We note that in other studies the attenuation relationship was determined for a relatively large distance range. In this example, the distance range applied in the regression, based on least-squares fits, executed by Shapira (1981) for Nevada nuclear explosions observed at WWSSN was up to 1000 km, and that of Hutton & Boore (1987), using a simple two-parameter regression, for earthquakes in southern California was up to 700 km.

We applied a two-step regression method, similar to that of

Joyner & Boore *et al.* (1981), for the attenuation function estimation (second term in eq. 1). Based on all observations, we incorporate the results of the regression n, k and S_i to obtain the attenuation function:

$$(1.850 \pm 0.005) \log R + (0.00460 \pm 0.00005) R \log e + 0.05 . \quad (2)$$

Since all the earthquakes occurred at shallow depths, the contribution of the depth is minor. The standard deviation of eq. (2) is 0.24 (or an uncertainty factor of 1.7). We have assumed that the attenuation property, in the frequency band of the short-period observations, is independent of the magnitude and source-to-station azimuth. We executed several regressions to verify this assumption (Fig. 3a). In the first test we limited ourselves to a distance of up to 500 km regardless of the source-to-station azimuth, and we obtained the attenuation function

$$(1.96 \pm 0.0004) \log R + (0.00530 \pm 0.00005) R \log e + 0.06 ; \quad (2A)$$

the standard deviation is 0.29. It is obvious that the results are dominated by the events that occurred south or west of the observing stations. In the other test we compared two main paths, namely, a continental path associated with events that occurred in the Arabian Shield east of the observing stations (Fig. 1), and to the west, an intermediate to oceanic path underlain by a thick sedimentary layer (Makris *et al.* 1994) associated with events that occurred in the Eastern Mediterranean. We limited ourselves to epicentres within a distance of 500 km. For the continental path, associated with efficient L_g propagation, we obtained (Fig. 3a)

$$(1.652 \pm 0.020) \log R + (0.0113 \pm 0.003) R \log e + 0.08 . \quad (2B)$$

The relatively large standard deviation of 0.51 is probably due to the small number of events (only eight). Extending the distance to about 1500 km yields a similar attenuation function with smaller standard deviation of 0.40. For the oceanic path, associated with efficient S_n propagation, we obtained (Fig. 3a)

$$(1.911 \pm 0.005) \log R + (0.00512 \pm 0.00005) R \log e + 0.06 ; \quad (2C)$$

the standard deviation is 0.23. Extending the distance to about 1000 km yields a similar attenuation function and slightly smaller standard deviation of 0.22. Despite the different propagation paths of the waves, travelling through the continental crust of the Arabian Shield to the east or the intermediate crust of the Mediterranean Sea to the west, it is clear that from a statistical point of view that they are rather similar. Thus we can conclude that eq. (2) serves as a representative attenuation function for the region (see Fig. 3a).

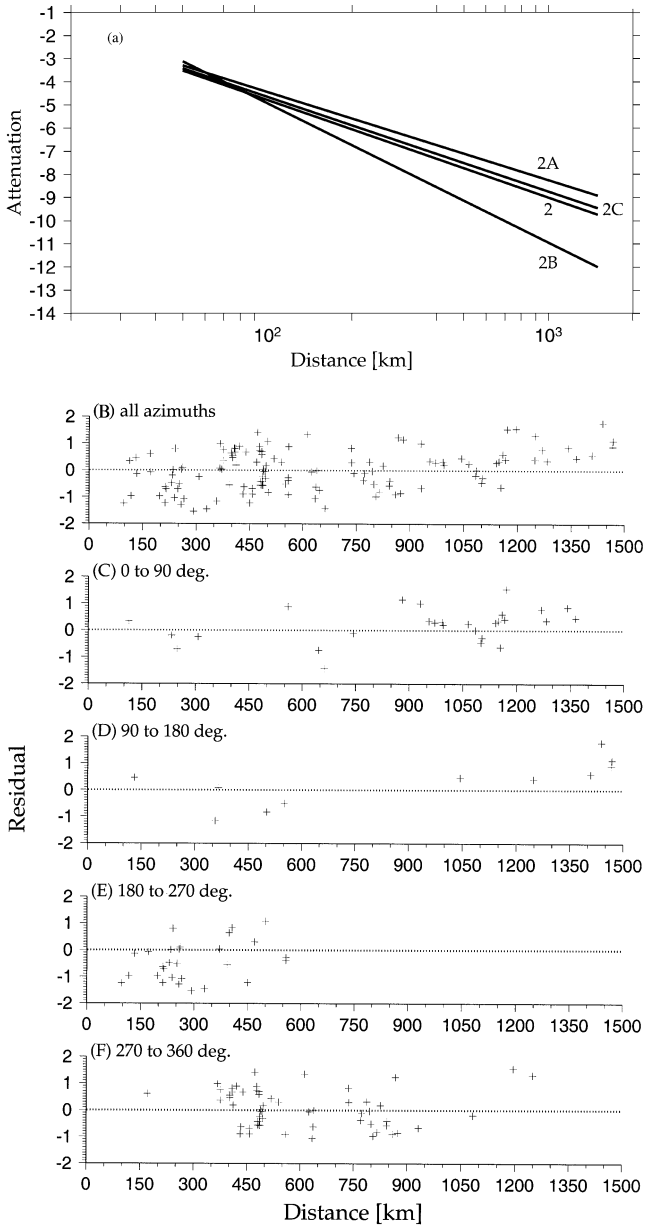

Figure 3. (a) Attenuation curves (dB) as a function of distance; the numbers close to the lines refer to the equations in the text. Residual of the attenuation versus the distance, binned by the azimuth: (b) all azimuths; (c) azimuthal gap 0°–90°; (d) azimuthal gap 90°–180°; (e) azimuthal gap 180°–270°; (f) azimuthal gap 270°–360°. Distance was calculated relative to the centre of the seismic network.

Figs 3(b)–(f) illustrate the residual of the attenuation as a function of the distance, which was also binned by azimuth, including the station correction (Table 1). Cases B (all directions), C (0°–90°) and F (270°–360°), which have a reasonable distribution of earthquake location relative to the observing stations with distance, suggest no distance dependence up to a distance of 1200 km, and a probable slight dependence beyond that up to a distance of 1500 km. Cases D (90°–180°) and E (180°–270°), although containing a relatively small number of events and limited to a distance range of 100 km to almost 600 km, respectively, suggest a similar behaviour. In order to investigate the distance dependence of the attenuation function for distances beyond 1200 km, we applied the t distribution (Jeffreys 1967) for several cases. For the cases B (all azimuths; essentially cases C and D), C (0°–90°), and D (90°–180°), which include a small number of degrees of freedom—9, 3 and 4 respectively—we obtained t-values of 6, 4 and 5, respectively, implying a probability of about 0.99. Thus, it appears as if there is distance dependence beyond a distance of 1200 km. Since the number of degrees of freedom is rather small, it is obvious that more observations in this distance range are needed to verify that we did not encounter a rare statistical case.

ENERGY DETERMINATION AND ENERGY–MAGNITUDE RELATIONSHIP

Once we determine the attenuation function we can estimate the energy observed at each station of a given event. We need

to execute the time-domain integration of the sum squared ground-motion velocity of the *S* wave, in a similar manner to the procedure proposed by Kanamori *et al.* (1993). The seismic energy observed at a given station starting at the *S* wave, E_S, using a window that includes all or most of the *S*-wave energy is

$$E_S = \frac{4\pi\rho_0\beta}{C_f^2}\int \sum v_S^2\, dt = 30.5\times 10^5 \int \sum v_S^2\, dt\,, \qquad (3)$$

neglecting the *P*-wave energy since it is a small fraction ($\approx$4 per cent) of the *S*-wave energy (Haskell 1964), where v_S is the particle motion velocity at the station, ρ_0 is the mass density of 2.5 g cm^{-3}, C_f is the free-surface amplification factor of 2, β is the *S*-wave velocity of 3.6 km s^{-1} (Ginzburg *et al.* 1979a,b) and E_S is given in ergs. The magnitude of most of the events is $m_B \geq 3.5$ or the corner frequency $f_0 \leq 2$ Hz. In the case of the relatively small events with $M_0 \approx 10^{21}$ dyn cm and $\Delta\sigma \approx 10$ bars (Table 2; see also Shapira & Hofstetter 1992), we obtain $f_0 \approx 3$ Hz. Thus, in order to estimate 80 per cent of the radiated energy (Singh & Ordaz 1994), the upper boundary of the frequency range over which the integration is being executed should be up to $f = 6f_0$. This range is included within the effective frequency range of the ISN seismometers (see Lee & Stewart 1981; van Eck & Hofstetter 1989).

The second step of the regression is the determination of the seismic energy–magnitude relationship, after considering the attenuation correction due to the distance. The energy at the source, E_0, was calculated using eqs (2) and (3). The correlation with the body wave magnitude m_R is

$$\log E_0 = (2.09 \pm 0.10) m_B + (8.86 \pm 0.42)\,. \qquad (4)$$

The standard deviation in estimating log E_0 is 0.78 (Fig. 4). In this regression, and also in those below, we take into account the fact that both m_B and E_0 are subject to errors, in a manner that is described by Draper & Smith (1981, Chapter 2). The latter showed that the fitting is adequate, since the spread in m_B is large compared with the spread of errors. In Fig. 4, and also in the remaining figures, we distinguished between earthquakes that are characterized by continental paths and those that are characterized by oceanic paths. We did not observe any trend due to the different paths. The energy–magnitude relationship is similar to those obtained by Thatcher & Hanks (1973) and Kanamori *et al.* (1993) for earthquakes in California. The 1995 November 22 event with $m_B = 6.2$ (the one with the arrow in Fig. 4) reflects the known m_B saturation at high values of body wave magnitude (Thatcher & Hanks 1973; Hanks & Kanamori 1979). It should be noted that assuming a high-order dependence on m_B would not significantly reduce the scatter in E_0. As discussed below, use of the moment magnitude, M_W, is preferred over the body wave magnitude, which reaches saturation at high values.

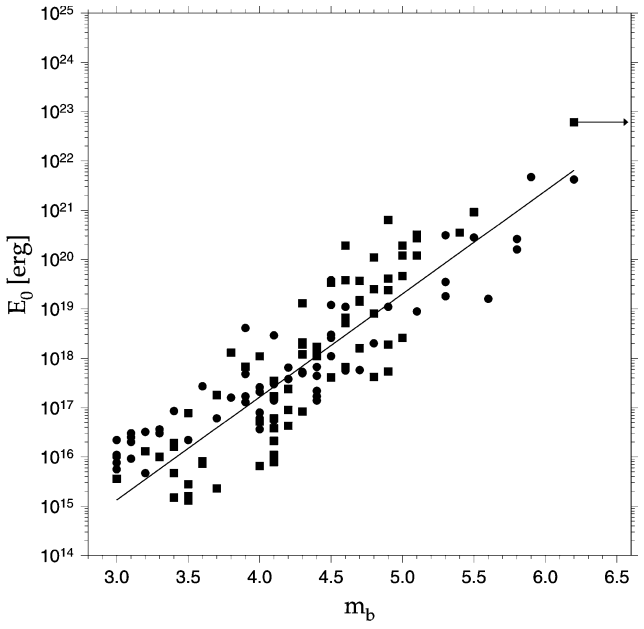

Figure 4. Energy as a function of body wave magnitude, m_B, obtained using the three-component short-period seismograms. Solid circles represent observations with oceanic paths and solid squares represent observations with continental paths (this is the same in all the other figures).

SEISMIC MOMENT AND STRESS DROP ESTIMATION

Our next step is to examine the relationships between the seismic energy and various seismic parameters, such as magnitude and seismic moment. We calculated the seismic moment (based on the dislocation model of Brune 1970) using the ISN observations (Shapira & Hofstetter 1992). The empirical regression between M_0 and m_B is

$$\log M_0 = (1.59 \pm 0.07) m_B + (15.63 \pm 0.28)\,, \qquad (5)$$

where M_0 is in dyn cm, the body wave magnitude range is $3.0 \leq m_B \leq 6.2$, and the observed standard deviation is 0.51 (Fig. 5). Combining eqs (4) and (5) we find that the relationship of seismic energy to seismic moment is $E_0 \propto M_0^{1.3}$, implying dependence on the size of the earthquake.

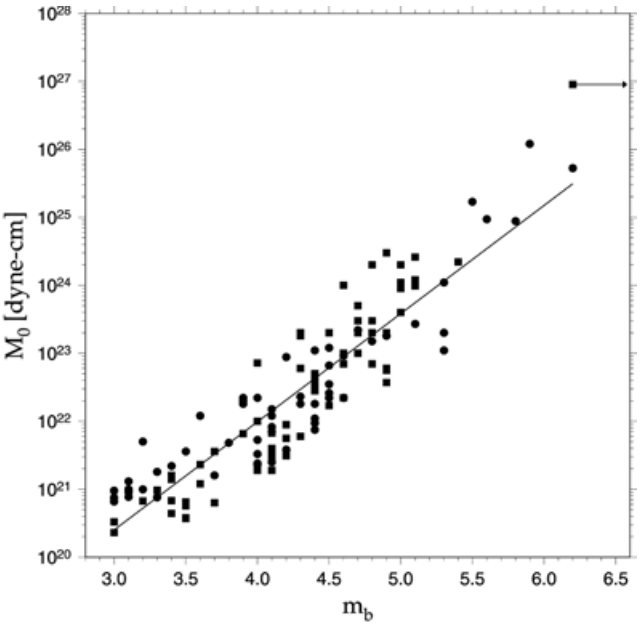

Figure 5. The relationship between the seismic moment and the body wave magnitude.

Orowan (1960) suggested a simple faulting model in which the stress drop $\Delta\sigma$ is from an initial stress σ_0 to a final stress σ_1 with a frictional stress σ_f. If the final stress is equal to the frictional stress, we obtain

$$\frac{E_0}{M_0} = \frac{\Delta\sigma}{2\mu}, \tag{6}$$

where μ is the rigidity. Following Orowan's (1960) model we plot lines of constant stress drop between 3 and 300 bars (Fig. 6). The seismic energy increases with M_0 following the relationship

$$\log E_0 = (1.19 \pm 0.04) \log M_0 - (8.81 \pm 0.83), \tag{7}$$

where the standard deviation of $\log E_0$ is 0.47. Several points should be mentioned here. The first is that the seismic energy increases with M_0, following the relationship $E_0 \propto M_0^{1.19}$, similar to above-mentioned value. The second point is that the Orowan stress drop varies from 1 bar to about 300 bars. Moreover, it implies that the Orowan stress drop increases with the seismic moment as $M_0^{0.19}$. We did not observe any azimuthal dependence, and thus we believe that it is a source effect. This phenomenon is in a good agreement with the recent studies of Thio (1995) for earthquakes in southern California, Mayeda & Walter (1996) for earthquakes in western USA and Castro *et al.* (1997) for the Friuli 1976 earthquake sequence in Italy.

Kanamori (1977), using a global earthquake data set, and Hanks & Kanamori (1979), using earthquakes in California, proposed the relationship $\log M_0 = 1.5 M_W + 16.1$, where M_W is the moment magnitude. Recently, Shapira & Hofstetter (1992) showed that this relationship holds for earthquakes in Israel and adjacent regions. Based on this relationship, and following the definition of energy-based magnitude M_E of Kanamori (1977) and Mayeda & Walter (1996), we obtain

$$M_E = \frac{2}{3} \log_{10} E_0 - 7.87, \tag{8}$$

which is simply related to the moment magnitude M_W:

$$M_E = M_W + \frac{2}{3} \log_{10} \left(\frac{\Delta\sigma}{2\mu} \right) + 2.87. \tag{9}$$

Kanamori (1977) and Mayeda & Walter (1996) showed that the main advantage in using both magnitude scales is that they are based on physical quantities that will not saturate. Whilst the estimation of the seismic moment is a relatively straightforward procedure, the seismic energy estimation is more complicated since it is dependent on the timescale of the energy release. Fig. 7 presents the relationship between M_E and M_W for the events in the data set, where the magnitude values were independently determined from the seismograms. The results suggest that the stress drop increases with moment for relatively low values of $M_W < 5$ and remains relatively constant for values of $M_W > 5.5$.

We estimate the stress drop of earthquakes $\Delta\sigma$, based on the dislocation model of Brune (1970), using the equation $\Delta\sigma = 8.47 M_0 f_0^3/\beta^3$, where f_0 is the corner frequency. Shapira & Hofstetter (1992) give details of the application of the method in the case of seismograms observed by the ISN (short period or broad band). In the case of strong earthquakes ($m_B > 5.0$), we use broad-band observations for calculating the stress drop. The stress drop clearly increases with increasing seismic moment (Fig. 8) or with seismic energy (Fig. 9) up to about 30 bars. On the other hand, relatively large values (>40 bars) are less common and there is no clear correlation between these values and the energy or seismic moment. The relatively large values of stress drop (>100 bars) are associated with seismic activity in the Hellenic or Cyprean arcs and the Zagros Mountains.

We compare the relationship of energy to seismic moment following the Orowan (1960) model (eq. 6) with the apparent stress $\sigma_a = \mu E_0/M_0$ (Wyss 1970) to obtain $\sigma_a = \Delta\sigma/2$ (Vassiliou & Kanamori 1982; Singh & Ordaz 1994; Castro *et al.* 1997) and presented in Fig. 10(a). A high proportion of the earthquakes surrounds the line $\sigma_a = \Delta\sigma/2$, suggesting a complete stress drop

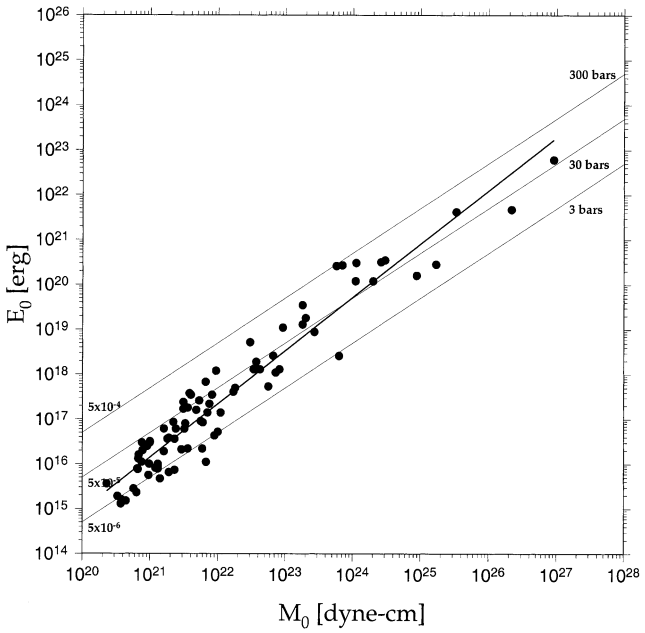

Figure 6. The energy release versus the seismic moment.

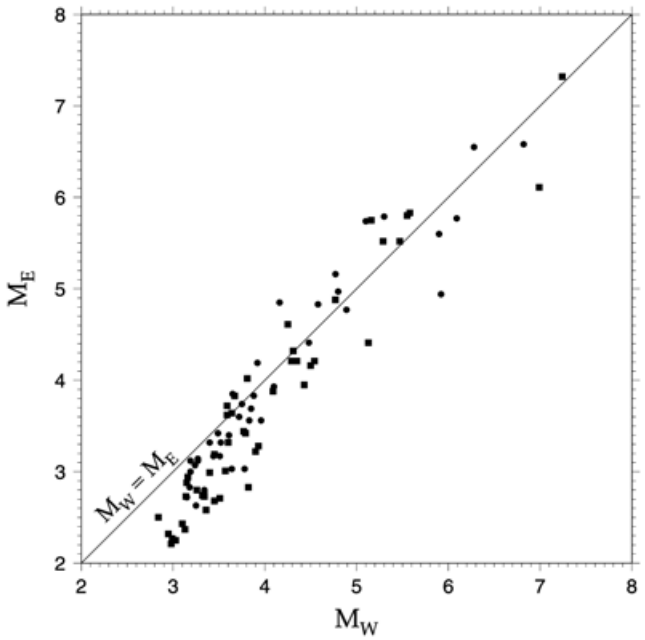

Figure 7. The relationship between M_E and M_W for the observed earthquakes.

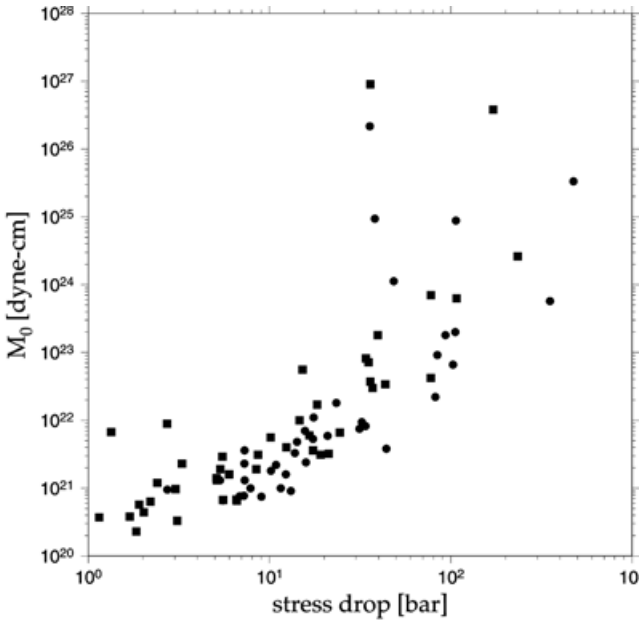

Figure 8. The relationship between Brune's stress drop $\Delta\sigma$ and the seismic moment M_0 for the events in this study.

following Orowan's model. The scattering in the seismic energy estimation (eq. 7) can explain the deviation of the nearby points from this line. Generally, the distribution of the points on both sides of the line $\sigma_a = \Delta\sigma/2$, and especially the distant ones, appears to be non-uniform, which suggests neither the situation $\sigma_a > \Delta\sigma/2$, the case of the partial stress drop model (Brune 1970), or the opposite case of $\sigma_a < \Delta\sigma/2$, which is the overshoot model (Savage & Wood 1971). The results were sorted into several groups according to the tectonic regions, that is the Eastern Mediterranean region, the Arabian Shield

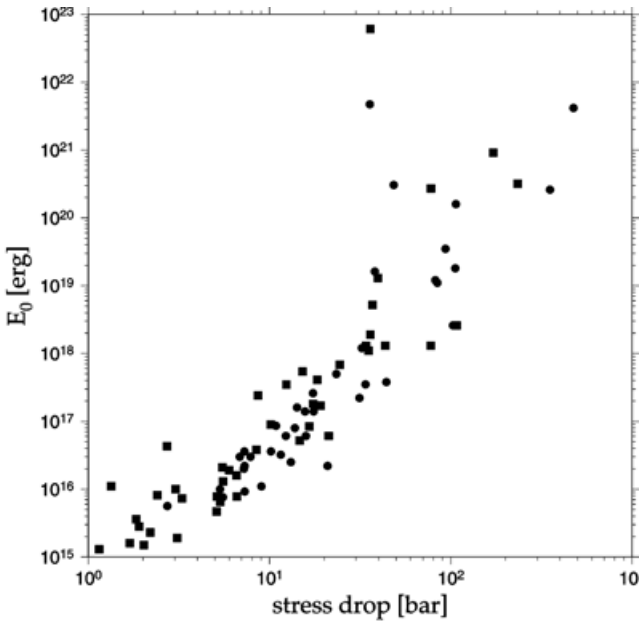

Figure 9. The relationship between Brune's stress drop $\Delta\sigma$ and the seismic energy E_0 for the events in this study.

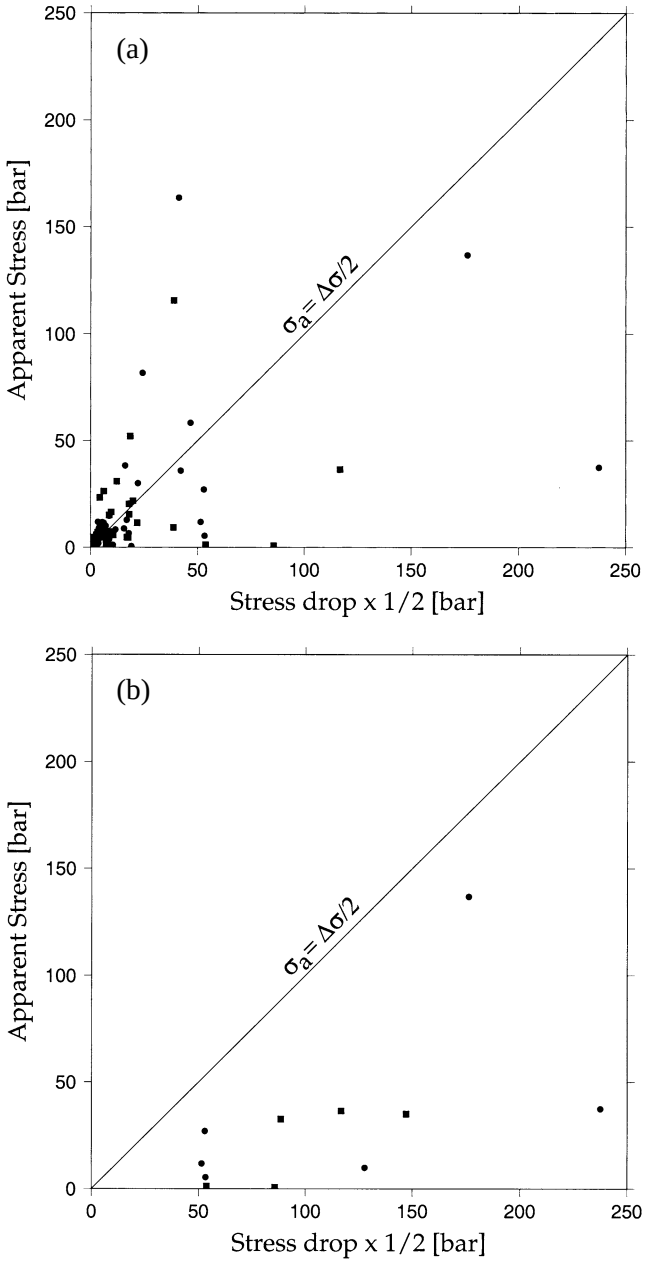

Figure 10. (a) Stress drop (half-value) versus apparent stress for all the earthquakes in this study. (b) Using only the earthquakes with large stress drop (>100 bars) in the Hellenic Arc and the Zagros Mountains.

and the Dead Sea rift, including the Gulf of Aqaba and the Red Sea. We did not observe any obvious pattern characterizing any of these regions. We performed another test selecting only the earthquakes with large values of stress drop (>100 bars), which included the events in the Hellenic or Cyprean arcs and the Zagros Mountains. Those regions are characterized by a compressional regime (McKenzie 1978; Jackson & McKenzie 1988). In this case we obtained a clear distribution of $\sigma_a < \Delta\sigma/2$ (Fig. 10b), favouring the overshoot model (Savage & Wood 1971). Results of other studies do not provide conclusive answers. For example, Singh & Ordaz (1994) reported that for Mexican data the Brune spectra in the frequency range $1 < f < 10$ Hz, assuming a complete stress drop of ≈ 120 bars,

fit the observed spectra well, and the median apparent stress is 24 bars. Mayeda & Walter (1996), using Californian data, could not fit a simple comparison of dynamic and static stress drops. Castro *et al*. (1997), using Friuli data, observed that most of the events seem to follow the partial stress drop model (Brune 1970).

CONCLUSIONS

We estimated the energy radiated by earthquakes that occurred in the Eastern Mediterranean region at varying distances, using the observed seismograms of short-period observations of the ISN. The attenuation function is determined to be $(1.850 \pm 0.005) \log R + (0.00460 + 0.00005)R \log e + 0.05$ for the distance range $50 \leq R \leq 1500$ km. The seismic energy estimation based on the method of Kanamori *et al*. (1993) is proportional to the integral of the velocity squared. The dependence of the attenuation function on the azimuth and distance is tested. From a statistical point of view we obtain similar results, despite the different propagation paths of the waves, travelling through the intermediate crust of the Mediterranean Sea to the west or the continental crust of the Arabian Shield to the east. For the magnitude range $3.0 \leq m_B \leq 6.2$, we obtained the magnitude–energy relationship $\log E_0 = (2.09 \pm 0.10)m_B + (8.86 \pm 0.42)$. The seismic energy increases with seismic moment approximately as M_0, following the relationship $E_0 \propto M_0^{1.19}$, and the Orowan stress drop increases with moment as M_0, following the relationship $M_0^{0.19}$, which is in general agreement with other recent studies.

ACKNOWLEDGMENTS

D. Kadosh, D. Levi, U. Peled and Y. Schwartz kept the ISN operating. C. Ben-Sasson, L. Feldman and B. Reich carried out the initial data processing. This study is supported by the Earth Science Research Administration, Ministry of the National Infrastructure. Figures in this report were prepared using the GMT program (Wessel & Smith 1991).

REFERENCES

Bath, M., 1966. Earthquake energy and magnitude, in *Contributions in Geophysics: In Honor of Beno Gutenberg,* eds Benioff, M.E., Howell, B.F. & Press, F., Pergamon Press, New York.

Boatwright, J. & Choy, G., 1986. Teleseismic estimates of the energy radiated by shallow earthquakes, *J. geophys. Res.,* **91,** 2095–2112.

Brune, J., 1970. Tectonic stress and the spectra of seismic shear waves from earthquakes, *J. geophys. Res.,* **73,** 4997–5009.

Castro, R., Pacor, F. & Petrungaro, C., 1997. Determination of S-wave energy release of earthquakes in the region of Friuli, Italy, *Geophys. J. Int.,* **128,** 399–408.

Draper, N. & Smith, H., 1981. *Applied Regression Analysis,* 2nd edn, John Wiley and Sons, New York.

El-Isa, Z., 1990. Lithospheric structure of the Jordan-Dead Sea transform from earthquake data, *Tectonophysics,* **180,** 29–36.

El-Isa, Z., Mechie, J., Prodehl, C., Makris, J. & Rihm, R., 1987. A crustal structure study of Jordan derived from seismic refraction data, *Tectonophysics,* **138,** 235–253.

GII Seismological Bulletins, 1984–98. *Earthquakes in and Around Israel,* Vol. 3–14, Seismological Division, Institute for Petroleum Research and Geophysics, Holon, Israel.

Ginzburg, A. & Gvirtzman, G., 1979. Changes in the crust and in the sedimentary cover across the transition from the Arabian Platform to the Mediterranean Basin: evidence from seismic refraction and sedimentary studies in Israel and Sinai, *Sed. Geol.,* **23,** 19–36.

Ginzburg, A., Makris, J., Fuchs, K., Perathoner, B. & Prodehl, C., 1979b. Detailed structure of the crust and upper mantle along the Jordan-Dead Sea rift, *J. geophys. Res.,* **84,** 5605–5612.

Ginzburg, A., Makris, J., Fuchs, K., Prodehl, C., Kaminski, W. & Amitai, U., 1979a. A seismic study of the crust and upper mantle of the Jordan-Dead Sea rift and their transition toward the Mediterranean Sea, *J. geophys. Res.,* **84,** 1569–1582.

Gutenberg, B. & Richter, C., 1942. Earthquake magnitude, intensity, energy and acceleration, 1, *Bull. seism. Soc. Am.,* **32,** 163–191.

Gutenberg, B. & Richter, C., 1956a. Earthquake magnitude, intensity, energy and acceleration, *Bull. seism. Soc. Am.,* **46,** 105–145.

Gutenberg, B. & Richter, C., 1956b. Magnitude and energy of earthquakes, *Ann. Geophys.,* **9,** 1–15.

Hanks, T.C. & Kanamori, H., 1979. A moment magnitude scale, *J. geophys. Res.,* **84,** 2348–2350.

Haskell, N., 1964. Total energy and energy spectral density of elastic wave radiation from propagating faults, *Bull. seism. Soc. Am.,* **56,** 1811–1842.

Hutton, K. & Boore, D., 1987. The M_L scale in Southern California, *Bull. seism. Soc. Am.,* **77,** 2074–2094.

Jackson, J. & McKenzie, D., 1988. The relationship between plate motions and moment tensors, and the rates of active deformation in the Mediterranean and Middle East, *Geophys. J. Int.,* **93,** 45–73.

Jeffreys, H., 1967. *Theory of Probability,* Oxford University Press, London.

Joyner, W. & Boore, D., 1981. Peak horizontal acceleration and velocity from strong-motion records, including records from the 1979 Imperial Valley, California, earthquake, *Bull. seism. Soc. Am.,* **71,** 2011–2038.

Kanamori, H., 1977. The energy release in great earthquakes, *J. geophys. Res.,* **82,** 2981–2987.

Kanamori, H., Mori, J., Hauksson, E., Heaton, T., Hutton, K. & Jones, L., 1993. Determination of earthquakes energy release and M_L using TERRAscope, *Bull. seism. Soc. Am.,* **83,** 330–346.

Lee, W.H.K. & Stewart, S., 1981. *Principles and Applications of Microearthquake Network,* Academic Press, New York.

Lindenfeld, M. & Berckhemer, H., 1995. Seismic energies of earthquakes and relationships to other source parameters, *Tectonophysics,* **248,** 171–184.

Makris, J., Ben-Avraham, Z., Behle, A., Ginzburg, A., Giese, P., Steinmetz, L., Whitmarsh, R. & Eleftheriou, S., 1983. Seismic refraction profiles between Cyprus and Israel and their interpretation, *Geophys. J. R. astr. Soc.,* **75,** 575–591.

Makris, J., Wang, S., Odintsov, S. & Udintsev, G., 1994. The magnetic field of the Eastern Mediterranean Sea, in *Geological Structure of the Northern Mediterranean,* pp. 75–87, eds Krasheninnikov, V. & Hall, J., Historical Productions–Hall, Jerusalem.

Mayeda, K. & Walter, R., 1996. Moment, energy, stress drop, and source spectra of Western United States earthquakes from regional coda envelopes, *J. geophys. Res.,* **101,** 11 195–11 208.

McKenzie, D., 1978. Active tectonics of the Alpine–Himalayan belt: the Aegean Sea and surrounding regions, *Geophys. J. R. astr. Soc.,* **55,** 217–254.

Orowan, E., 1960. Mechanism of seismic faulting, *Geol. Soc. Am.,* **79,** 323–345.

Rodgers, A., Ni, J. & Hearn, T., 1997. Propagation characteristics of short-period S_n and L_g in the Middle East, *Bull. seism. Soc. Am.,* **87,** 396–413.

Sandvol, E., Seber, D., Barazangi, M., Mohamad, R., Türkelli, N., Gürbüz, C., Zor, E. & Gök, R., 1998. Seismological research in the Middle East, in *Proc. 20th Ann. seism. Res. Symp. on CTBT*, pp. 526–535, eds Fantroy, J., Heatley, D., Warren, J., Chavez, F. & Meade, C., Santa-Fe.

Savage, J. & Wood, M., 1971. The relation between apparent stress and stress drop, *Bull. seism. Soc. Am.,* **61,** 1381–1388.

Shapira, A., 1981. Regional coda magnitudes of underground nuclear explosions, *Phys. Earth planet. Inter.,* **26,** 188–197.

Shapira, A., 1988. Magnitude scales for regional earthquakes monitored in Israel, *Isr. J. Earth Sci.,* **37,** 17–22.

Shapira, A. & Hofstetter, A., 1992. Source parameters and scaling relationships of earthquakes in Israel, *Tectonophysics,* **217,** 217–226.

Shaw, B., 1998. Far-field radiated energy scaling in elastodynamic earthquake fault models, *Bull. seism. Soc. Am.,* **88,** 1457–1465.

Singh, S. & Ordaz, M., 1994. Seismic energy release in Mexican subduction zone earthquakes, *Bull. seism. Soc. Am.,* **84,** 1533–1550.

Thatcher, W. & Hanks, T., 1973. Source parameters of southern California earthquakes, *J. geophys. Res.,* **78,** 8547–8576.

Thio, H.-K., 1995. Using short-period surface waves to study seismic source and structure, *PhD thesis,* California Inst. Technology, CA.

Thio, H.-K., Saikia, C., Woods, B., Helmberger, D. & Hofstetter, R., 1998. Path calibration for broadband IMS stations in the Mediterranean region, North Africa and the Middle East, in *Proc. 20th Ann. seism. Res. Symp. on CTBT,* pp. 146–155, eds Fantroy, J., Heatley, D., Warren, J., Chavez, F. & Meade, C., Santa-Fe.

Van Eck, T. & Hofstetter, A., 1989. Microearthquake activity in the Dead Sea region, *Geophys. J. Int.,* **99,** 605–620.

Vassiliou, M.S. & Kanamori, H., 1982. The energy release in earthquakes, *Bull. seism. Soc. Am.,* **72,** 371–387.

Wessel, P. & Smith, W., 1991. Free software helps maps and display data, *EOS, Trans. Am. geophys. Un.,* **72,** 441.

Wyss, M., 1970. Stress estimates for South American shallow and deep earthquakes, *J. geophys. Res.,* **75,** 1529–1544.